3D Quantum-inspired Self-supervised Tensor Network for Volumetric Segmentation of Brain MR Images

Debanjan Konar [1,1,1], Siddhartha Bhattacharyya [2], Tapan Kumar Gandhi [2], Bijaya Ketan Panigrahi [2], and Richard Jiang [2]

[1]Indian Institute of Technology Delhi
[2]Affiliation not available

November 8, 2023

Abstract

This paper introduces a novel shallow self-supervised tensor neural network for volumetric segmentation of brain MR images obviating training or supervision. The proposed network is a 3D version of the Quantum-Inspired Self Supervised Neural Network (QIS-Net) architecture and is referred to as 3D Quantum-inspired Self-supervised Tensor Neural Network (3D-QNet). The underlying architecture of 3D-QNet is composed of a trinity of volumetric layers viz. input, intermediate and output layers inter-connected using a 26-connected third-order neighborhood-based topology for voxel-wise processing of 3D MR image data suitable for semantic segmentation. Each of the volumetric layers contains quantum neurons designated by qubits or quantum bits. The incorporation

of tensor decomposition in quantum formalism leads to faster convergence of the network operations to preclude the inherent slow convergence problems faced by the self-supervised networks. The segmented volumes are obtained once the network converges. The suggested 3D-QNet is tailored and tested on the BRATS 2019 data set extensively in the experiments carried out. 3D-QNet has achieved promising dice similarity while compared with the intensively supervised convolutional network-based models 3D-UNet, Vox-ResNet, DRINet, and 3D-ESPNet, thus facilitating annotation free semantic segmentation using a self-supervised shallow network.

3D Quantum-inspired Self-supervised Tensor Network for Volumetric Segmentation of Medical Images

Debanjan Konar, *SMIEEE,* Siddhartha Bhattacharyya, *SMIEEE,* Tapan K. Gandhi, *SMIEEE,*
Bijaya K. Panigrahi, *SMIEEE,* and Richard Jiang, *SMIEEE*

Abstract—This paper introduces a novel shallow 3D self-supervised tensor neural network for volumetric segmentation of medical images with merits of obviating training and supervision. The proposed network is referred to as the 3D Quantum-inspired Self-supervised Tensor Neural Network (3D-QNet). The underlying architecture of 3D-QNet is composed of a trinity of volumetric layers viz. input, intermediate, and output layers inter-connected using an $\mathcal{S}$-connected third-order neighborhood-based topology for voxel-wise processing of 3D medical image data, suitable for semantic segmentation. Each of the volumetric layers contains quantum neurons designated by *qubits* or quantum bits. The incorporation of tensor decomposition in quantum formalism leads to faster convergence of the network operations to preclude the inherent slow convergence problems faced by the classical supervised and self-supervised networks. The segmented volumes are obtained once the network converges. The suggested 3D-QNet is tailored and tested on the BRATS 2019 Brain MR image data set and Liver Tumor Segmentation Challenge (LiTS17) data set extensively in our experiments. 3D-QNet has achieved promising dice similarity as compared to the time intensive supervised convolutional neural network-based models like 3D-UNet, Vox-ResNet, DRINet, and 3D-ESPNet, thereby showing a potential advantage of our self-supervised shallow network on facilitating semantic segmentation.

Index Terms—Quantum Computing, Volumetric Medical Image Segmentation, QIS-Net, Tensor Network

I. Introduction

Automatic volumetric medical image segmentation assisted by contextual information yields Volumes of Interest (VOIs), which are critical to cancer patients. Deeply supervised Convolutional Neural Networks (CNN) have achieved respectable accuracy in 2D medical image segmentation [1]–[4]. However, in automatic 3D medical image data segmentation, deeply supervised 3D-CNNs suffer from manually affected challenges viz. acquiring sufficient 3D annotated data for suitable training, high heterogeneity and dimensionality of 3D medical images, complex anatomical environments, and the need for optimizing the 3D neural networks [5]–[7]. Hence, 3D medical imaging research calls for self-supervised learning

D. Konar is with the CASUS - Center for Advanced Systems Understanding, Helmholtz-Zentrum Dresden-Rossendorf (HZDR), Görlitz, Germany, Email: d.konar@hzdr.de

T. K. Gandhi, and B. K. Panigrahi are with the Department of Electrical Engineering, Indian Institute of Technology Delhi, New Delhi, India, Email: tgandhi@ee.iitd.ac.in and bkpanigrahi@ee.iitd.ac.in

S. Bhattacharyya is with Rajnagar Mahavidyalaya, Birbhum, West Bengal, India, Email: dr.siddhartha.bhattacharyya@gmail.com

R. Jiang is with the School of Computing and Communications, Lancaster University, Lancaster, UK, Email: r.jiang2@lancaster.ac.uk

for accurate and fast segmentation of volumetric medical images with different modalities.

The unified concept of quantum-inspired neural networks (QINN) enhances the approximation and generalization capabilities of classical neural networks and has emerged to process information faster in the field of computer science [8], [9]. Of late, quantum-inspired neural networks are becoming popular in solving problems in the domain of pattern recognition and classification [10], [11], [14], [15], employing the inherent characteristics of quantum computation. However, the complex and time-intensive quantum back-propagation algorithm in the aforementioned QINN models suffers from slow convergence problems. In addition, the fixed activation schemes adopted in the QINN models restrict their application to gray-scale image segmentation.

Given 3D medical image data, the primary aim of our proposed 3D-QNet architecture is to perform volumetric organ and lesions segmentation with expert-level accuracy for tumor identification alleviating supervision or training. Our proposed 3D-QNet architecture centres on the self-supervised bi-directional counter propagation of the quantum states obviating the time-intensive quantum back-propagation algorithm for faster convergence. The network hyper-parameters associated with the gray-level thresholding process are adaptive, and voxel-wise context-sensitive information is exhibited in quantum formalism, as reported in this article.

Translational medicine (TM) is an emerging concept and practice that facilitates the rapid transfer of medical breakthroughs from scientists to clinicians. Recently, there have been a number of instructive instances in which the translation of research has resulted in undesirable effects needing prompt intervention [12], [13]. A greater emphasis on three-dimensional (3D) simulation, biomarkers, and artificial intelligence may enable orthopaedic surgeons to forecast the optimal surgical techniques prior to surgery. Utilizing the most advanced imaging methods may enhance the precision and accuracy of tumor resections. This article is aimed at young surgeon scientists, specifically orthopaedic residents, to help them better understand how 3D quantum-inspired models can be used to process high mega pixel volumetric medical images in a faster, self-supervised manner, with merits of obviating training or very limited training. Heuristically, the suggested 3D-QNet has the ability to investigate the inherent features of quantum parallelism in order to concurrently compute high-resolution image voxels. This expedites the transfer of

information from the laboratory to the patient's bedside.

The current voxel-wise segmentation work has significant contributions over 2D medical image segmentation [1]–[3], [14] as given below.

1) We propose a novel quantum-inspired self-supervised shallow voxel-wise neural network referred to as 3D-QNet, which has relevance on volumetric medical image segmentation.

2) In this work, an $\mathcal{S}$-connected quantum fuzzy context-sensitive voxel information is processed to integrate the appearance of low-level and high-level local image features with wide intensity variations and implicit shape of the VOIs, thereby enabling accurate volumetric segmentation of 3D medical images.

3) A novel generalized quantum-inspired self-supervised learning is proposed using a tensor representation of the weight vectors for high dimensional data employed in our suggested 3D-QNet for 3D medical image segmentation. The non-tensorized implementation of 3D-QNet, referred to as 3D-QNet-NonTensor, is also demonstrated in our experiments.

4) The convergence analysis of the proposed 3D-QNet is also demonstrated with super-linearity. The primary aim of incorporating quantum computing in our proposed 3D network architecture is to exploit the features of quantum correlation and accelerate the speed of convergence of the network operation, thereby simultaneously improving the discrimination ability to yield fast and accurate segmentation.

The organization of the remaining sections of the manuscript is as follows: a comprehensive literature review about various deep learning-based volumetric segmentation of medical images and the challenges are presented in Section II. Section III illustrates the fundamental concepts of quantum computing. The novel self-supervised 3D-QNet architecture with a quantum-inspired tensor network model is introduced in Section IV. Section V elucidates voxel-wise segmentation of 3D medical images using the proposed 3D-QNet architecture. The experimental datasets, experimental setup, and outcome are provided in Section VI. The advantages and limitations of the proposed work have been discussed in Section VII. Section VIII states the concluding remarks of the proposed work and sheds light on the future directions of research.

II. RELATED WORKS

Recent years have witnessed a surge in the application of deep learning networks in various tumor segmentation [16]–[20] tasks with respectable accuracy in 2D medical image segmentation [2], [21]. However, in contrast to automated volumetric segmentation of medical images, 2D convolutional neural network architectures (CNNs) [16], [18], [19] process the medical images in a 2D independent slice-wise fashion which leads to non-optimal use of the 3D contextual feature information of volumetric medical image data (3D Computed Tomography (CT) and Magnetic Resonance Imaging (MRI)). In turn, 3D CNN based architectures extract rich spatial and contextual features and perform voxel-wise segmentation of volumetric medical images [22]–[24]. Kamnitas *et al.* [22] suggested a dual path 3D CNN incorporating local and larger contextual feature information to obviate the computationally complex 3D medical image processing and exhibit dense inference on medical image segmentation. A flexible network, 3D-UNet architecture [24] achieved remarkable success on brain MR image semantic segmentation. Of late, to exploit the 3D contextual information, Brebisson *et al.* [25] employed 2D CNNs on three orthogonal 2D patches and formed 3D patches in combination to reduce the memory requirements. However, 3D CNN networks suffer from slow convergence problems owing to computationally exhaustive 3D convolution operations and extensive training procedures. Despite popularity among the medical and computer vision researchers, U-Net architectures [24] fall short in scalability and cannot distinguish the distinctive features (shape, size, intensity, location etc.) learned at the convolutional layers. Moreover, they suffer from the vanishing gradient problem when the number of feature layers is increased to better represent the features. Various deeper network architectures obviating the vanishing gradient problem have been proposed concurrently for voxel-wise medical image segmentation including VoxResNet [26], DRINet [27], and 3D-ESPNet [28].

However, these deeply supervised network architectures suffer in computational complexity and slow-convergence with an increase in the number of feature layers in the network architecture. Currently, self-supervised/semi-supervised/weakly supervised networks have gained significant attention among the computer vision and medical imaging research community due to lack of annotated images for deep supervision [29]–[32]. Nevertheless, these self-supervised networks [29]–[32] for volumetric medical image segmentation rely on pre-trained 3D CNN models, and hence these are not fully self-supervised networks. Moreover, these networks are characterized by significant memory footprints which often poses a serious obstacle in employing them in various medical imaging application settings. It inspires us to develop 3D self-supervised neural network architectures for volumetric medical image segmentation.

The main problem with the classical self-supervised neural network models lies in the fact that they do not converge fast and hence the segmented outcome is distorted due to the slower convergence problems [33], [34]. Numerous quantum neural networks have been evolved in the last few decades replicating classical neural networks and offering faster processing while compared with the classical counterparts [9], [35]–[38]. The quantum versions of the classical self-supervised neural network architectures [10], [11], [39], [40] offer a potential candidate for faster and efficient image segmentation and surpasses the classical counterparts. Konar *et al.* recently developed quantum-inspired neural network models referred to as QIS-Net [14], QFS-Net [15], and QIBDS-Net [41] suitable for brain MR image segmentation. These networks have been found to attain a promising outcome in complete brain tumor segmentation and serve as the motivation behind the assimilation of quantum-inspired computing in the current 3D-QNet architecture.

This manuscript presents a novel fully 3D self-supervised

quantum-inspired shallow neural network architecture for volumetric medical image segmentation to obviate the comprehensive challenges faced by deep supervision of complex 3D CNNs.

III. FUNDAMENTALS OF QUANTUM COMPUTING

The basic concept of quantum computing deals with the principles of quantum mechanics and offers to demonstrate the quantum computing algorithms which rely on quantum bits having quantum operations on *qubits* [42].

A. Quantum Bits and Tensor Products

The basic element equivalent to classical bits in quantum computing is known as quantum bit or *qubit* and is represented using *Dirac* notations $|0\rangle$ and $|1\rangle$. However, unlike classical computing, quantum bits are expressed as a linear combination of probability amplitudes often known as superposition as follows [9].

$$|\phi\rangle = \cos\frac{\alpha}{2}|0\rangle + e^{i\frac{\theta}{2}}\sin\frac{\alpha}{2}|1\rangle \tag{1}$$

where, $0 \leq \alpha \leq \pi$ and $0 \leq \theta \leq 2\pi$.

Hence, *qubits* reside in the Hilbert space parametrized by the continuous variables θ and α. In quantum formalism, the *tensor products* of the subspace form the full Hilbert space, H as

$$H = \otimes_{t=1}^{n} H_t \tag{2}$$

A set of n basis states (designated as $|\phi_j\rangle$) comprising $0 - 1$ can form a *qubit* system $|\psi\rangle$, of size $\log n$ in the Hilbert space, H as follows.

$$|\psi\rangle = \sum_{j}^{n} p_j|\phi_j\rangle \tag{3}$$

where, p_j is the probability amplitude and $|\phi_j\rangle = |\phi_1\rangle \otimes |\phi_2\rangle \otimes \ldots |\phi_n\rangle$. For example, using two *qubits*, four distinct tensor sub-spaces can be created as basis $|0\rangle \otimes |0\rangle$, $|0\rangle \otimes |1\rangle$, $|1\rangle \otimes |0\rangle$ and $|1\rangle \otimes |1\rangle$ often represented as $|00\rangle$, $|01\rangle$, $|10\rangle$, and $|11\rangle$, respectively.

B. Input Data Encoding and Tensor Decomposition

A tensor product basis relies on the local input feature map $\{\mathbf{\Phi}^{d_j}(\alpha_j)\}$ in the Hilbert space of functions over $\alpha_j \in [0,1]$ as [38]

$$|\mathbf{\Phi}^{d_1,d_2,\ldots d_N}(\boldsymbol{\alpha})\rangle = |\phi^{d_1}(\alpha_1)\rangle \otimes |\phi^{d_2}(\alpha_2)\rangle \otimes \ldots \otimes |\phi^{d_N}(\alpha_N)\rangle \tag{4}$$

where, d_j varies from $1 \ldots N$ (N-dimensional vector). A function, $f^l(\boldsymbol{\alpha})$ can be realized using the inner product of the input local feature map $\phi^{d_j}(\alpha_j)$ and the network weight decomposition $\mathbf{\Psi}$, as follows.

$$f^l(\boldsymbol{\alpha}) = \langle \mathbf{\Psi}^l | \mathbf{\Phi}(\boldsymbol{\alpha})\rangle$$
$$= \langle \mathbf{\Psi}_{d_1 d_2 \ldots d_N} |\phi(\alpha_1^{d_1})\rangle \otimes |\phi(\alpha_2^{d_2})\rangle \ldots \otimes |\phi(\alpha_N^{d_N})\rangle \tag{5}$$

Hence, the local feature map $\phi^{d_j}(\alpha_j)$ forms a basis for a Hilbert space of functions defined over $\alpha \in [0,1]$ and the tensor product basis $\mathbf{\Phi}^{d_1,d_2,\ldots d_N}(\boldsymbol{\alpha})$ forms a Hilbert space of

functions defined over $\alpha \in [0,1]^N$. Considering the dimensions of the input feature vector restricted to $N = 2$, $\phi(\alpha)$ is defined as

$$\phi(0) = [0,1], \ \phi(1) = [1,0] \tag{6}$$

To enhance and extract the contextual information from high dimensional data, Tucker tensor decomposition is suitable for neural network layer decomposition [43]. The inner product of the two equal sized tensors $\mathbf{V}, \mathbf{\Psi} \in \mathbb{R}^{m \times n \times p}$ is defined as follows.

$$|\boldsymbol{\xi}\rangle = \langle \mathbf{V}|\mathbf{\Psi}\rangle = \sum_l \langle \mathbf{V}^{(l)}, \mathbf{\Psi}^{(l)}\rangle = \sum_{i=1}^{M} \theta_i|i\rangle \cdot \sum_{j=1}^{N} \phi_j|j\rangle$$
$$= \begin{pmatrix} \theta_1 \\ \theta_2 \\ \vdots \\ \theta_M \end{pmatrix} \cdot \begin{pmatrix} \phi_1 \\ \phi_2 \\ \vdots \\ \phi_N \end{pmatrix}, \theta_i \in \mathbf{V}, \ \phi_j \in \mathbf{\Psi} \tag{7}$$

IV. 3D QUANTUM-INSPIRED SELF-SUPERVISED TENSOR NEURAL NETWORK (3D-QNET) ARCHITECTURE

In this article, a 3D Quantum-inspired Self-supervised Tensor Network (3D-QNet) architecture with self-supervised tensor learning is proposed for automatic voxel-wise segmentation of medical images. The 3D-QNet architecture comprises a trinity of volumetric layers of quantum neurons arranged as input, intermediate and output layers. A schematic outline of the proposed 3D-QNet architecture is shown in Figure 1. The input volume ($M \times N \times P$) is normalized and propagated from the 3D input layer to the successive 3D hidden and output layers of the 3D-QNet architecture for processing through $\mathcal{S}$-connected voxels. Each of the three volumetric layers of the 3D-QNet architecture is fully intra-linked with *qubits* using a 3D-matrix representation. Each 3D layer of the proposed architecture is intra-connected through quantum neurons with intra-connection strengths set to $\frac{\pi}{2}$ (quantum 1 logic). The basic processing unit of each volumetric layer of the 3D-QNet architecture is the $\mathcal{S}$-connected neighborhood-based voxel-wise orientation of each candidate neuron as illustrated in Figure 2. The inter-layer connection between the 3D input to 3D intermediate and the 3D intermediate to 3D output layer is formed using the $\mathcal{S}$-connected voxel-wise neighborhood orientation. The contribution of the $\mathcal{S}$ number of neighborhood quantum neurons (pixels) of a candidate neuron at one 3D layer is propagated in the forward direction and accumulated at the corresponding candidate neuron of the subsequent 3D layer. Consequently, the voxel-wise information from the 3D output layer to the 3D intermediate layer is counter-propagated for further processing. The voxel-wise processing of each 3D layer is performed along with the depth of the 3D layer for semantic segmentation. The inter-linked connections between two successive 3D layers are represented using 3D weight matrices of *qubits* and each inter-connection weight is updated using rotation gate for faster processing. The relevant details about the principle of operation of the proposed 3D-QNet architecture for volumetric segmentation are provided in the following subsections using a self-supervised tensor learning model in quantum formalism.
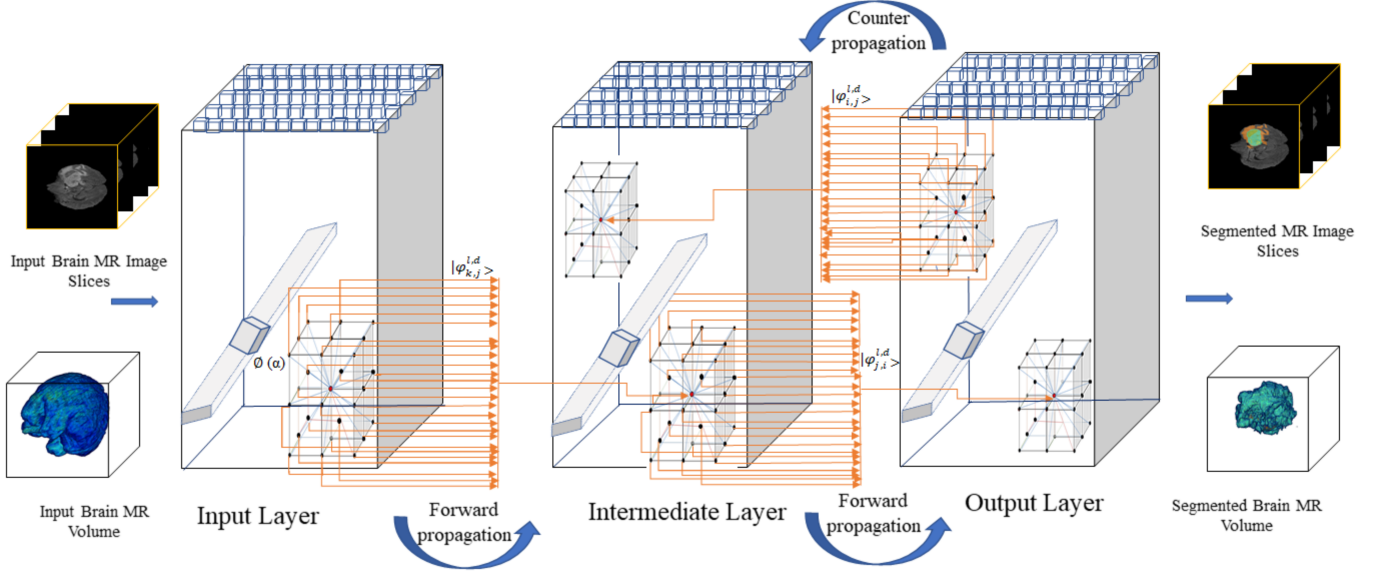
Fig. 1: 3D Quantum-inspired Self-supervised Tensor Neural Network (3D-QNet) architecture. For every candidate neuron as marked in red color, it forms a $\mathcal{S}$-connected neighborhood oriented Inter-layer connections and here only three Inter-layer connection is illustrated for better visibility. A classical information, α is mapped to quantum bits or qubits as, $\phi(\alpha) = \left[\cos(\frac{\pi}{2}\alpha) \ \sin(\frac{\pi}{2}\alpha)\right]$. The inter-connection weights between the input and hidden layers of the 3D-QNet architecture are denoted by $|\varphi_{k,j}^{l,d}\rangle$, for the hidden layers to the output layers are indicated by $|\varphi_{j,i}^{l,d}\rangle$ and for the output to the hidden layers are $|\varphi_{i,j}^{l,d}\rangle$ at a layer l with depth d. The classical interconnection weight $[0,1]$ is transformed in quantum formalism as $|\varphi(\omega)\rangle = \left[\cos(\frac{\pi}{2}\omega) \ \sin(\frac{\pi}{2}\omega)\right]$, where the angle of rotation (ω) is measured using the relative difference of fuzzy intensities of the candidate pixel and the neighborhood pixels in $\mathcal{S}$-connected (here, $\mathcal{S} = 26$) neighborhood oriented quantum neurons in a $3 \times 3 \times 3$ voxel (v) as $\omega_{i,j} = 1 - (\alpha_i - \alpha_{i,j}); j \in \{1,2,3,\ldots\mathcal{S}\}$. 3D-volumes of dimensions $3 \times 3 \times 3$ are processed along the depth of the 3D-layers as shown in the Figure.
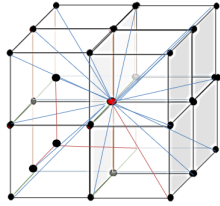

Fig. 2: $\mathcal{S}$-connected neighborhood oriented quantum neurons form a voxel (The red pixel is the candidate neuron and the black pixels represent the corresponding neighborhood neurons).

A. 3D-Quantum-Inspired Self-supervised Tensor Network Model

In the suggested 3D-QNet architecture, the high dimensional weight vector $\mathbf{\Psi}$ is represented using a tensor to optimize the network operations and to facilitate the extraction of significant semantic feature information in the quantum-inspired self-supervised model. The internal kernels associated with the network operate in parallel, thereby accelerating convergence of the 3D-QNet architecture. The input quantum neurons containing the pixel intensity are expressed as *qubits* and the inter-connection weights are represented using quantum rotation gates. The classical intensity of any i^{th} normalized gray-scale image pixel of MR or CT volume (denoted as $\alpha_i \in [0,1]$) is transformed into quantum state using a mapping

function $\phi(\alpha_i)$ as follows.

$$\phi(\alpha_i) = \left[\cos(\frac{\pi}{2}\alpha_i) \ \sin(\frac{\pi}{2}\alpha_i)\right] \forall i = 1, \ldots M, j = 1, \ldots N \tag{8}$$

The classical interconnection weight $[0,1]$ is transformed into quantum formalism as

$$|\boldsymbol{\varphi}(\omega_{i,j})\rangle = \left[\cos(\frac{\pi}{2}\omega_{i,j}) \ \sin(\frac{\pi}{2}\omega_{i,j})\right] \tag{9}$$

Hence, the strength of inter-connection between neuron j (neighborhood of the candidate neuron i) of a layer to the corresponding candidate neuron of the adjacent layer is mapped using φ. Also, $\omega_{i,j}$ is designated as the angle of rotation and measured as the relative intensity difference between the candidate pixel (α_i) and one of its neighborhood pixels $\alpha_{i,j}$ as follows.

$$\omega_{i,j} = 1 - (\alpha_i - \alpha_{i,j}); j \in \{1,2,3,\ldots\mathcal{S}\} \tag{10}$$

The angle of rotation is measured using the relative difference of fuzzy intensities of the candidate pixel and the neighborhood pixels in quantum formalism. This relative measure encoding scheme [14], [15], [39] helps to segment the foreground and background regions of an image. However, there are other encoding schemes like variational and amplitude encoding, which are often used for variational quantum circuits.

In this proposed tensor network model, the 3D-QNet layer is decomposed as voxel (core tensor) using Tucker Tensor decomposition [43] to reduce the input dimensions and the

interconnection wights as factor matrices. Let us consider tensor $\mathcal{V}, \Psi \in \mathbb{R}^{m \times n \times p}$, where $\mathcal{V}$ is the voxel-wise input of 3D medical images and the corresponding inter-connection 3D weight matrix is evaluated in Eq. 9, respectively (m, n, p denote the row, column, and slice number. $\mathcal{V}, \Psi$ are third-order tensors ($1 \leq m \leq M, 1 \leq n \leq N, 1 \leq p \leq P$)). According to Tucker Tensor decomposition [43]

$$\mathcal{X} = \mathcal{V} \times_1 \mathbf{\Psi}^1 \times_2 \mathbf{\Psi}^2 \times_3 \mathbf{\Psi}^3 \quad (11)$$

where, $\mathcal{X} \in \mathbb{R}^{m \times n \times p}$ is the tensor outcome, Ψ^n is the weight matrix in terms of n factor matrix and $\times_n$ is the $mod - n$ product of a tensor with a matrix. Each layer of the proposed 3D-QNet architecture is transformed to lower-dimensional tensors. Such types of $M \times N \times P$ tensors in voxel form each layer in the underlying network architecture. Each volumetric layer of the 3D-QNet architecture forms $M \times N \times P$ volumetric patches (voxels) of size $\mathcal{S}$ corresponding to the candidate pixels as

$$\boldsymbol{v} = vox(\mathcal{V}) \quad (12)$$

Here, $\mathcal{V}$ comprises all the 3D-patches (voxels), $\boldsymbol{v} \in \mathbb{R}^{m \times n \times p}$ for a network layer in the proposed 3D-QNet architecture. The spatial features in terms of the neighborhood pixels of every seed pixel at the network layer, are extracted and propagated to the next subsequent layers as inputs guided by a Quantum-inspired voxel-wise multi-level Sigmoidal (Vox-QSig) activation function, $\sigma_{3D-QNet}$ as follows.

$$\boldsymbol{y}^l = \sigma_{3D-QNet}(\boldsymbol{v}^{l-1} \cdot \mathbf{\Psi}^l(\omega)) \quad (13)$$

where, $\boldsymbol{v}^{l-1} \in \mathbb{R}^{M \times N \times P}$, $\mathbf{\Psi}^l(\omega) \in \mathbb{R}^{M \times N \times P \times \mathcal{S}}$ at the network layer $l = 2, 3$, $\boldsymbol{y}^l \in \mathbb{R}^{\mathcal{S}}$, and "·" is the inner product operator. The Vox-QSig activation function, $\sigma_{3D-QNet}$ with slope λ and activation ϑ, is defined as

$$\sigma_{3D-QNet}(x) = \frac{1}{\beta_\tau + e^{-\lambda(x-\vartheta)}}, 0 \leq \beta_\tau \leq \frac{\pi}{2} \quad (14)$$

where, β_τ describes the multi-level class responses exhibited by the $\mathcal{S}$-connected third-order neighborhood pixels expressed as

$$\beta_\tau = \frac{\chi_\mathcal{S}}{\rho_\tau - \rho_{\tau-1}} \quad (15)$$

where, ρ_τ and ρ_τ are the τth and $(\tau - 1)^{th}$ class outcome, respectively and the contribution of the $\mathcal{S}$-connected neighborhood gray-level pixels is $\chi_\mathcal{S}$.

The fuzzy context-sensitive activation (designated as χ_i) for semantic segmentation in quantum formalism is defined as follows.

$$|\chi_i\rangle = \begin{bmatrix} \cos \vartheta_i \\ \sin \vartheta_i \end{bmatrix} \quad (16)$$

where, the angle of rotation, ϑ_i is evaluated using the summation of the intensities of the third-order $\mathcal{S}$-connected neighborhood pixels (denoted as $\alpha_{i,j}, j = 1, 2, \ldots \mathcal{S}$) of a candidate pixel i (neuron) in quantum formalism using the following equation.

$$\vartheta_i = 2\pi \times (\sum_{j=1}^{\mathcal{S}} \alpha_{i,j}) \quad (17)$$

TABLE I: Variational parameters used in the counter-propagation algorithm of the proposed 3D-QNet

Symbol	Description
$\alpha_i^{l,d}$	The intermediate output at pixel i at layer l and depth d
$\omega^{l,d}$	The rotation angle for inter-connection weight at layer l with depth d
$\chi_\mathcal{S}$	It corresponds the contribution of $\mathcal{S}$-connected third-order neighborhood pixels
ϑ_i^l	The fuzzy context sensitive activation in quantum formalism at layer l
$\delta_i^{l,d}$	The phase transformation parameters at layer $l-1$ with depth d

Quantum fuzzy context-sensitive thresholding determines the bi-directional propagation of quantum information between the layers of the 3D-QNet architecture by means of self-organization of the inter-linked weight matrices. Reduction of feature dimensions using tensor decomposition followed by voxel-wise information processing of the proposed 3D-QNet architecture is inspired by the basic quantum neural network input-output model [14] as follows.

$$|\phi^l(\alpha_i^d)\rangle = \sigma_{3D-QNet}\Big(\sum_j^{m \times n \times p} f^{l-1}(\alpha_i^d)\langle \varphi_j^l | \chi_i^{l,d}\rangle \Big) \quad (18)$$

where, $|\phi^l(\alpha_i^d)\rangle$ denotes the intermediate output of the ith seed quantum neuron at the 3D network layer in the lth sample with depth (slice#) $d = 1, 2, \ldots P$. $\sigma_{3D-QNet}$ is the Quantum-inspired voxel-wise multi-level Sigmoidal activation (Vox-QSig) function with activation as $|\chi_i^{l,d}\rangle$. The output $|\phi^l(\alpha_i^d)\rangle$ can be written as

$$|\phi^l(\alpha_i^d)\rangle =$$
$$f\Big(\frac{\pi}{2}\delta_i^{l,d} - \arg\Big\{ \sum_j^{m \times n \times p} f^l(\omega_{j,i}^d)f^{l-1}(\alpha_i^d) - f^l(\chi_i^d)\Big\}\Big)$$
$$= \sigma_{3D-QNet}\Big(\sum_j^{m \times n \times p} f^{l-1}(\alpha_i^d)(\cos(\omega_{j,i}^{l,d} - \vartheta_i^l) +$$
$$\gamma \sin(\omega_{j,i}^{l,d} - \vartheta_i^l))\Big) \quad (19)$$

Here, the designated rotation angles associated with the inter-connection weights between input neuron j to output neuron i are represented by $\omega_{j,i}^{l,d}$ and $\delta_i^{l,d}$ is the phase transfer parameter. The variational parameters used in the counter-propagation algorithm are provided in Table I. The true classical output state ($|1\rangle$) from the ith quantum neuron is obtained by considering the imaginary part (sin) of the above expression where, γ is an imaginary unit. Assume that the inter-connection weights between the input and hidden layers of the 3D-QNet architecture are denoted by $|\varphi_{k,j}^{l,d}\rangle$ and for the hidden layer to the output layer, are indicated by $|\varphi_{j,i}^{l,d}\rangle$ in the lth sample sets. The activation at the hidden and output layers are designated using $|\chi_j^{l,d}\rangle$ and $|\chi_i^{l,d}\rangle$, respectively. Considering any quantum

seed neuron k from the sample of input neurons at the input layer, the corresponding seed neuron at the hidden layer be j and the output seed neuron be i, the response at the ith neuron with depth d in the lth sample sets is expressed as

$$|\phi^l(\alpha_i^d)\rangle = \sigma_{3D-QNet}(\sum_j^{m\times n\times p} f(\frac{\pi}{2}y_j^{l,d})\langle\varphi_{ji}^{l,d}|\vartheta_j^{l,d}\rangle)$$

$$= \sigma_{3D-QNet}(\sum_j^{m\times n\times p} f(\frac{\pi}{2}\times\sigma_{3D-QNet}(\sum_k^{m\times n\times p} f(\frac{\pi}{2}y_j^{l,d}) \\ \langle\varphi_{kj}^{l,d}|\vartheta_k^{l,d}\rangle)\langle\varphi_{ji}^{l,d}|\vartheta_j^{l,d}\rangle) \quad (20)$$

i.e.,

$$|\phi^l(\alpha_i^d)\rangle = \sigma_{3D-QNet}(\sum_j^{m\times n\times p}$$

$$f(\frac{\pi}{2}\times\sigma_{3D-QNet}(\sum_k^{m\times n\times p} f(\frac{\pi}{2}y_j^{l,d})\cos(\omega_{k,j}^{l,d}-\vartheta_j^{l,d})$$

$$\cos(\omega_{j,i}^{l,d}-\vartheta_i^{l,d})+\gamma\sin(\omega_{k,j}^{l,d}-\vartheta_j^{l,d})\sin(\omega_{j,i}^{l,d}-\vartheta_i^{l,d})))))$$
$$(21)$$

where, γ is an imaginary number.

B. Quantum-inspired Voxel-wise multi-level Sigmoidal (Vox-QSig) activation function

In this 3D-QNet architecture, a Quantum-inspired Voxel-wise multi-level Sigmoidal (Vox-QSig) activation function is proposed for voxel-wise processing of $\mathcal{S}$-connected spatially oriented neighborhood-based pixels. The generalized form of the Vox-QSig activation function is obtained by leveraging the activation function hyper-parameters employed in Equation 14 as

$$\sigma_{Vox-QSig}(x;\beta_\tau,\rho_\tau) = \sum_{\tau=1}^L \frac{1}{\beta_\tau + e^{-\lambda(x-(\tau-1)\rho_{\tau-1}-\vartheta)}} \quad (22)$$

where, L corresponds to the number of class levels. The multi-class responses for various hyper-parameters employed in the Vox-QSig activation functions are provided in Figure 3.

C. Adjustment of Inter-connection Weights of 3D-QNet and Loss Function

Each inter-connection link for each candidate pixel of the $\mathcal{S}$-connected medical image volume and its corresponding activation are updated using quantum rotation gates, thereby enabling faster convergence of the proposed 3D-QNet architecture. The inter-connection weight, $\varphi^{l,d}$ and its activation, $\chi^{l,d}$ are updated as follows.

$$|\varphi^{\iota+1,d}\rangle = \begin{pmatrix} \cos\triangle\omega^{\iota+1,d} & -\sin\triangle\omega^{\iota+1,d} \\ \sin\triangle\omega^{\iota+1,d} & \cos\triangle\omega^{\iota+1,d} \end{pmatrix}|\varphi^{\iota,d}\rangle \quad (23)$$

$$|\chi^{\iota+1,d}\rangle = \begin{pmatrix} \cos\triangle\vartheta^{\iota+1,d} & -\sin\triangle\vartheta^{\iota+1,d} \\ \sin\triangle\vartheta^{\iota+1,d} & \cos\triangle\vartheta^{\iota+1,d} \end{pmatrix}|\chi^{\iota,d}\rangle \quad (24)$$

where,

$$\omega^{\iota+1,d} = \omega^{\iota,d} + \triangle\omega^{\iota,d} \quad (25)$$

(a) $L = 3$ (b) $L = 5$
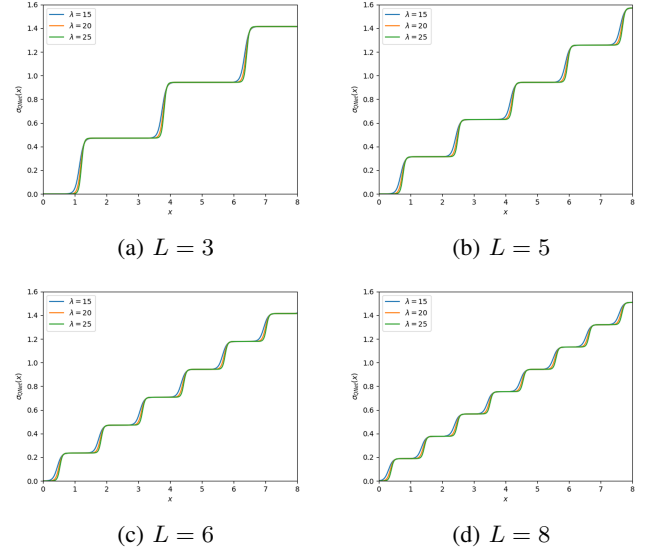
(c) $L = 6$ (d) $L = 8$

Fig. 3: Multi-level class response of *Vox-QSig* activation function for $\lambda = 15, 20, 25$.

and

$$\vartheta^{\iota+1,d} = \vartheta^{\iota,d} + \triangle\vartheta^{\iota,d} \quad (26)$$

Equations 25 and 26 refer to updating the angles of rotation and activation, respectively. The error or loss function, $\zeta(\omega^{\iota,d}, \vartheta^{\iota,d})$ in the suggested 3D-QNet architecture is evaluated in terms of Root Mean Square Error (RMSE) of the 3D-weight matrices at depth d (or the slice $\#d$) in the lth epoch and is defined on the phase angles $\omega^{\iota,d}, \vartheta^{\iota,d}$ as

$$\zeta(\omega^{\iota,d}, \vartheta^{\iota,d}) =$$

$$\frac{1}{\mathcal{N}} \sum_{i=1}^{\mathcal{N}} \sum_{j=1}^{\mathcal{S}} \left[\varphi_{ij}(\omega_{ij}^{\iota+1,d}, \vartheta_i^{\iota+1,d}) - \varphi_{ij}(\omega_{ij}^{\iota,d}, \vartheta_i^{\iota,d})\right]^2 \quad (27)$$

V. VOLUMETRIC MEDICAL IMAGE SEGMENTATION USING 3D-QNET

Minimum pre-processing is performed before the medical image slices are fed as inputs to 3D-QNet. The input medical image volume is normalized as a fuzziness measure ($[0, 1]$) before transforming it to *qubits* as follows.

$$\alpha_{i,j}^d = \frac{\alpha_{i,j}^d - min(\alpha_{i,j}^d)}{max(\alpha_{i,j}^d) - min(\alpha_{i,j}^d)} \quad (28)$$

Medical image volumes exhibit heterogeneous responses over the local intensities in the $\mathcal{S}$-connected neighborhood regions, owing to the wide variations of gray-levels. Inspired by the authors' previous works [14], [34], [44], the proposed *Vox-QSig* activation function employs four different adaptive thresholding schemes suitable for efficient gray-scale segmentation in the 3D-QNet architecture.
(1) Activation guided by β-distribution of the intensity of $\mathcal{S}$-connected neighborhood voxels (υ_β).
(2) Activation guided by $\mathcal{S}$-connected voxels based on Skewness (υ_χ).
(3) Activation guided by $\mathcal{S}$-connected heterogeneous voxel

intensities (v_ξ).

(4) Activation guided by $\mathcal{S}$-connected fuzzy voxel cardinality estimates (v_κ).

In addition, to investigate a number of optimal thresholds $\{\mathcal{T}_1, \mathcal{T}_2, \cdots, \mathcal{T}_{C_l-1}\}$ in multi-class settings, Otsu's method [45] is explored. The optimal thresholds maximize the class variance as follows [45].

$$\mathcal{O} = h_n\{\mathcal{T}_1, \mathcal{T}_2, \cdots, \mathcal{T}_{C_l-1}\}\theta_i(\mu_i - \omega) \qquad (29)$$

where, C_l represents the number of defined classes in $\mathcal{C}$ $=\{C_1, C_2, \ldots, C_{C_l}\}$ and

$$\theta_i = \sum_{i \in C_l} p_i \ , \ \mu_i = \sum_{i \in C_l} ip_i/\theta_l \qquad (30)$$

where, the ith pixel is defined as p_i. The probability of class C_i is represented as μ_i and its mean value is given by μ_i. ω is known to be the mean of class $\mathcal{C}$.

To refine the segmentation accuracy and dice score for false-positive reduction in brain tumor detection, 3D-QNet segmented highly representative volumetric intensity features are post processed using the k-Means algorithm [46] for initial label segmentation and segmented into pre-defined number of clusters.

VI. Results

A. Data Set

The proposed 3D-QNet and its non-tensorized implementation (3D-QNet-NonTensor) are validated extensively using the BRATS 2019 data set [47] and the Liver Tumor Segmentation Benchmark (LiTS17) data set [48]. The BRATS 2019 data set is composed of 315 (239 HGG and 76 LGG) 3D MRI volumes. Each MRI volume comprises 155 slices of resolution 240×240 with the ground truth segmented labels and includes four different modalities of 3D MR images viz. $T1$, $T1$ with Contrast-Enhanced ($T1 - CE$), $T2$, and $FLAIR$. The segmented labels are annotated with three distinct tumor sub-regions, viz. tumor core (TC), tumor enhancing (TE), necrosis and non-enhancing core region. These three annotations form a complete tumor (WT). The BRATS 2019 data set is divided into $8 : 2$ ratio for training (252) and testing (63) due to GPU limitations. The Liver Tumor Segmentation Benchmark (LiTS17) data set [48] consists of 131 CT scans with various types of tumors. The LiTS17 data set is also divided into $8 : 2$ ratio for training and testing in the study. Each CT volume consists of variable number of slices of resolution 512×512.

B. Experimental Setup

Experiments have been carried out using 3D-QNet and 3D-QNet-NonTensor on 3D brain MR volumes collected from the BRATS 2019 dataset of size 240×240 and on the LiTS17 data set of size 512×512 with MATLAB 2020a. The proposed 3D-QNet and 3D-QNet-NonTensor architectures are implemented with the multi-level gray-scale images using distinct multi-class levels $L = 4, 6$, and 8 characterized by the *Vox-QSig* activation function. The steepness λ is varied in the range 0.23 to 0.24 with step size of 0.001. For *FLAIR* and *T2*, it has

been observed that in majority of cases, $\lambda = 0.232$ and $\mathcal{S} = 26$ ($3 \times 3 \times 3$ volume) yield optimal performance. For the other two modalities *T1* and *T1-CE*, $\lambda = 0.238$ and $\mathcal{S} = 26$ ($3 \times 3 \times 3$ volume) yield optimal performance. On contrary, the LiTS17 CT volume data has performed optimally for $\lambda = 0.239$ and $\mathcal{S} = 26$ ($3 \times 3 \times 3$ volume). Moreover, the Vox-QSig is guided by four distinct activation schemes ($v_\beta, v_\xi, v_\zeta, v_\kappa$) [14], [34], [44]. Experiments have also been performed using the 3D-UNet [24] architecture, Deep Voxel-wise Residual Network (VoxResNet) [26], Dense-Res-Inception Net (DRINet) [27], and 3D-ESPNet [28] on the BRATS 2019 data set [47] and on the LiTS17 data set [48]. We have trained 3D-UNet [24] and VoxResNet [26] rigorously with the Stochastic Gradient Descent (SGD) algorithm on *Caffe* library[1] using an Nvidia Tesla $V100 - SXM2$ GPU Cluster with 32 GB of memory and 640 Tensor cores with 8 cores of Intel(R) Xeon(R) CPU E5-2683 v4@2.1GHz. The 3D-ESPNet is implemented using *Pytorch* from the code available in Github[2] with 100 epochs using *adam* optimizer with an initial learning rate of 0.01. The DRINet is also implemented using *adam* optimizer with an initial learning rate of 0.01 and kernel size of 3×3. In order to detect a complete tumor, the segmented output images are resized to match the binary mask's dimensions, with the result 1 representing the tumor region and 0 representing the backdrop. The dice similarity (DS) [18], which is regarded as a standard assessment technique in automatic medical image segmentation, can be evaluated by pixel to pixel comparison with manually segmented regions of interest or lesion mask. The ground truth for the evaluation is a manually segmented lesion mask, and each 2D pixel is predicted as True Positive (T_{RP}) or True Negative (T_{RN}) or False Positive (T_{RN}) or False Negative (F_{LN}). The empirical goodness measures [Positive Predictive Value (PV), Sensitivity (SS), Accuracy (AC) and Dice Similarity (DS) [18]] are assessed to evaluate the results.

C. Experimental Results

Experiments have been carried out in the current setup, and the results have been reported together with numerical and statistical analysis using the proposed 3D-QNet, 3D-QNet-NonTensor, 3D-UNet [24], VoxResNet [26], DRINet [27], and 3D-ESPNet [28] on BRATS 2019 data set [47] and LiTS17 data set [48]. Table II presents the complete tumor (WT) segmentation on BraTS19-CBICA-AAG-1-flair-slice#69. It is evident from the experimental data reported in Table II that the proposed 3D-QNet performs optimally for complete brain tumor segmentation of four different modalities of MR volumes (viz. $T1$, $T1 - CE$, $FLAIR$, and $T2$) using the activation guided by 26-connected heterogeneous voxel intensities (v_ξ) with $L = 8$ in comparison with other thresholding schemes under the four evaluation parameters (AC, DS, PV, SS) [18]. The 3D-QNet segmented brain MR slices collected from two different volumes *BRATS19-CBICA-AAG* and *BRATS19-CBICA-AAB* using class level $L = 8$ with activation scheme v_ξ, are shown in Figures 4 and

[1]https://doi.org/10.1145/2647868.2654889
[2]https://github.com/sacmehta/3D-ESPNet

5, respectively. The human expert annotated ground truth slices for all the four different modalities are illustrated in Figure 6. 3D-UNet [24], VoxResNet [26], DRINet [27], 3D-ESPNet [28], and 3D-QNet-NonTensor segmented brain MR volumes from *BRATS19-CBICA-AAG* are also demonstrated in the *Supplementary Materials*. It has been observed from the segmented MR slices that the proposed 3D-QNet is suitable in segmenting the correct position and size of the complete tumor while compared with the ground truth segmentation. However, it is not efficient in mapping the sharp contour of the core and enhanced tumor sub-regions outlined in the annotated slices. Table III presents the quantitative results reported using the proposed 3D-QNet, 3D-QNet-NonTensor, 3D-UNet [24], VoxResNet [26], DRINet [27], and 3D-ESPNet [28] on evaluating the average accuracy (AC), dice similarity score (DS), positive prediction value (PV), and sensitivity (SS) [18]. It has been observed from the 3D-QNet segmented brain MR slices and the results reported in Table III, that optimal segmentation is achieved for $FLAIR$ reported with an average of 0.821 dice score (DS). The proposed 3D-QNet marginally outperforms the convolutional architectures (3D-UNet [24], VoxResNet [26], DRINet [27], 3D-ESPNet [28]), and 3D-QNet-NonTensor in predicting complete brain tumor detection. However, it may be noted that the proposed 3D-QNet does not intend to predict the core, enhanced tumor and necrosis sub regions owing to lack of optimization of the parameters in the suggested 3D-QNet architecture. The box plots are also demonstrated in the *Supplementary Materials* citing the outcome reported in Table III. Moreover, to show the effectiveness of the proposed 3D-QNet architecture over 3D-UNet [24], VoxResNet [26], DRINet [27], and 3D-ESPNet [28], we have also conducted experiments on the Liver Tumor Segmentation Benchmark (LiTS17) data set [48]. Table IV presents the results reported using the proposed 3D-QNet, 3D-UNet [24], VoxResNet [26], 3D-QNet-NonTensor, DRINet [27], and 3D-ESPNet [28] on LiTS17 data set [48] in detecting complete Liver tumor regions. A sample of segmented Liver tumor using 3D-QNet with manually segmented tumors is shown in Figure 7. It is observed from Table IV that 3D-QNet has reported with an average Dice Score (DS) of 0.958. Furthermore, a one-sided two-sample Kolmogorov-Smirnov (KS) [49] test is performed with a significance level of $\alpha = 0.05$, and the experimental data given in Table III and Table IV show that 3D-QNet is capable of segmenting 3D medical image data. Despite being characterized by fully self-supervised quantum-inspired learning, the 3D-QNet has demonstrated comparable accuracy (AC) and dice similarity (DS) in comparison to 3D-UNet [24], VoxResNet [26], DRINet [27], and 3D-ESPNet [28]. Hence, the performance of the 3D-QNet model on the BRATS 2019 and LiTS17 data sets are statistically significant and offers a promising alternative to self-supervised deep learning for 3D-medical image segmentation. Furthermore, in case of brain MR image segmentation, the number of parameters required in the 3D-UNet [24] architecture is $19,069,955$, whereas the proposed 3D-QNet architecture employs maximum $2,995,200$ parameters (considering each voxel as a candidate in a 240×240 dimensional slice, there are total $240 \times 240 \times 26 \times 2$ connections) in bi-directional

propagation.

The convergence analysis of the proposed 3D-QNet architecture is discussed in the *Appendix* and experimentally demonstrated with the non-tensorized implementation of the network (3D-QNet-NonTensor). The convergence analysis of the proposed 3D-QNet and 3D-QNet-NonTensor architectures for all types of brain tumor images ($T1$, $T1 - CE$, $Flair$, and $T2$) from the BRATS 2019 datasets [47] and for LiTS17 liver volumes [48] are provided in the *Supplementary Materials*. Table V reports the average number of iterations required to converge the proposed 3D-QNet architecture and its non-tensorized implementation, 3D-QNet-NonTensor. It is evident from Table V that an optimal convergence of the proposed 3D-QNet architecture is observed for Flair with υ_ξ. Hence, the non-tensorized implementation (3D-QNet without tensor decomposition) underperforms in terms of average iterations in comparison to 3D-QNet. It serves as the inspiration behind the incorporation of tensor-decomposition in 3D-QNet implementation.

VII. Discussions

The proposed 3D-QNet is computed and tested on a classical system. Hence, the proposed model architecture is not quantum in the real sense. Instead, it is quantum-inspired. The pixel intensities and interconnection weight matrices are expressed in quantum formalism in classical simulations using real vectors. Here, each pixel information and weight term are presented as a vector with better expressibility and non-linearity than classical neurons. The 3D-QNet network architecture and the use of a unitary matrix representation in network weights ensure the authenticity of quantum analogies without sacrificing efficacy or efficiency, as shown by a full comparison with state-of-the-art models on two benchmark datasets. The incorporation of quantum-inspired computing and tensor-based learning in the suggested network model aims to provide faster convergence of the 3D-QNet architecture over its non-tensorized implementation, thereby enabling accurate segmentation results.

However, the proposed 3D-QNet architecture may be implemented utilizing a quantum-classical hybrid paradigm for NISQ devices on the real quantum processor. In this hybrid quantum classical framework, the $\mathcal{N}$-connected third-order neighborhood-based interconnection needed $\mathcal{N}$ (here $\mathcal{N} = 26$) input qubits, Hadamard gates, and Rotation gates, as well as $\mathcal{N}(\mathcal{N} - 1)$ numbers of CNOT gates [15], which resulted in quantum superposition and entanglement of the input states. This quantum-classical model lays the way for the implementation of quantum machine learning on near-term NISQ devices using variational quantum circuits (VQCs) — a kind of Quantum circuits with improved gate settings.

It is worth noting that 3D-QNet has the potential to be significantly more computationally efficient than the models presented in the experiments, especially in multi-level segmentation of BRATS 2019 MR images. The performance of many quantum-inspired algorithms derives directly from quantum parallelism, which is a fundamental characteristic of many quantum systems. Heuristically, the proposed 3D-QNet

TABLE II: Results obtained using proposed 3D-QNet for complete tumor (WT) segmentation on BraTS19-CBICA-AAG-1-flair-slice#69

Level	Modality	$AC = \frac{T_{RP}+T_{RN}}{T_{RP}+F_{LP}+T_{RN}+F_{LN}}$				$DS = \frac{2T_{RP}}{2T_{RP}+F_{LP}+F_{LN}}$				$PV = \frac{T_{RP}}{T_{RP}+F_{LP}}$				$SS = \frac{T_{RP}}{T_{RP}+F_{LN}}$			
		v_β	v_χ	v_ξ	v_κ	v_β	v_χ	v_ξ	v_κ	v_β	v_χ	v_ξ	v_κ	v_β	v_χ	v_ξ	v_κ
$L=4$	$T1$	**0.99**	**0.99**	**0.99**	**0.99**	0.62	**0.80**	**0.80**	0.79	0.44	**0.66**	0.65	0.65	**0.99**	**0.99**	**0.99**	**0.99**
	$T1-CE$	**0.99**	**0.99**	**0.99**	**0.99**	0.79	**0.80**	0.79	**0.80**	**0.66**	**0.66**	**0.66**	**0.66**	**0.99**	**0.99**	**0.99**	**0.99**
	$FLAIR$	**0.99**	**0.99**	**0.99**	**0.99**	0.62	**0.80**	**0.80**	0.79	0.44	**0.66**	**0.66**	0.65	**0.99**	**0.99**	**0.99**	**0.99**
	$T2$	**0.99**	**0.99**	**0.99**	**0.99**	0.62	**0.80**	**0.80**	0.79	0.44	**0.66**	**0.66**	0.65	**0.99**	**0.99**	**0.99**	**0.99**
$L=6$	$T1$	**0.99**	**0.99**	**0.99**	**0.99**	0.62	**0.80**	**0.80**	0.79	0.44	**0.66**	**0.66**	0.65	**0.99**	**0.99**	**0.99**	**0.99**
	$T1-CE$	**0.99**	**0.99**	**0.99**	**0.99**	0.62	**0.80**	**0.80**	0.79	0.44	**0.66**	**0.66**	0.65	**0.99**	**0.99**	**0.99**	**0.99**
	$FLAIR$	**0.99**	**0.99**	**0.99**	**0.99**	0.62	**0.80**	**0.80**	0.79	0.44	**0.66**	**0.66**	0.65	**0.99**	**0.99**	**0.99**	**0.99**
	$T2$	**0.99**	**0.99**	**0.99**	**0.99**	0.62	**0.80**	**0.80**	0.79	0.44	**0.66**	**0.66**	0.65	**0.99**	**0.99**	**0.99**	**0.99**
$L=8$	$T1$	**0.99**	**0.99**	**0.99**	**0.99**	0.82	**0.82**	**0.82**	0.81	**0.70**	0.69	0.69	0.68	**0.99**	**0.99**	**0.99**	**0.99**
	$T1-CE$	**0.99**	**0.99**	**0.99**	**0.99**	0.81	**0.81**	**0.81**	0.81	0.68	0.68	0.68	0.68	**0.99**	**0.99**	**0.99**	**0.99**
	$FLAIR$	**0.99**	**0.99**	**0.99**	**0.99**	0.84	**0.84**	**0.84**	0.84	0.73	0.73	0.73	0.72	**0.99**	**0.99**	0.98	0.98
	$T2$	**0.99**	**0.99**	**0.99**	**0.99**	0.82	**0.82**	**0.82**	0.82	0.69	0.69	**0.70**	**0.70**	**0.99**	**0.99**	**0.99**	**0.99**

TABLE III: Comparative analysis of proposed 3D-QNet with 3D-QNet-NonTensor, 3D-UNet [24], VoxResNet [26], DRINet [27], and 3D-ESPNet [28] [The bold numbers represent evaluation metrics completed with a one-sided two-sample KS test with a significance threshold of $\alpha = 0.05$ [49]]

Methods	Modality	AC	DS	PV	SS
3D-UNet [24]	$T1$	0.990	0.811	0.736	0.941
	$T1-CE$	0.990	0.807	0.732	0.938
	$FLAIR$	**0.992**	**0.823**	0.737	0.943
	$T2$	0.989	0.812	0.735	0.944
VoxResNet [26]	$T1$	0.990	0.810	0.737	0.937
	$T1-CE$	0.989	0.813	0.732	0.943
	$FLAIR$	**0.991**	**0.822**	**0.751**	0.942
	$T2$	0.990	0.807	0.729	0.944
DRINet [27]	$T1$	0.989	0.793	0.701	0.958
	$T1-CE$	0.988	0.800	0.711	0.959
	$FLAIR$	0.989	0.805	0.708	**0.969**
	$T2$	0.987	0.789	0.700	0.958
3D-ESPNet [28]	$T1$	0.989	0.801	0.709	0.961
	$T1-CE$	0.989	0.813	0.721	**0.966**
	$FLAIR$	0.989	0.800	0.715	0.959
	$T2$	0.988	0.802	0.714	0.957
3D-QNet	$T1$	0.989	0.801	0.736	**0.965**
	$T1-CE$	0.989	0.811	0.740	0.957
	$FLAIR$	**0.991**	**0.821**	**0.751**	0.957
	$T2$	0.990	0.814	0.736	0.960
3D-QNet-NonTensor	$T1$	0.987	0.776	0.678	0.959
	$T1-CE$	0.987	0.772	0.678	0.958
	$FLAIR$	0.989	0.786	0.697	0.956
	$T2$	0.988	0.788	0.696	0.957

TABLE IV: Comparative Results on Liver Segmentation using proposed 3D-QNet, 3D-UNet [24], VoxResNet [26], 3D-QNet-NonTensor, DRINet [27], and 3D-ESPNet [28] [The bold numbers represent evaluation metrics completed with a one-sided two-sample KS test with a significance threshold of $\alpha = 0.05$ [49]]

Methods	AC	DS	PV	SS
VoxResNet [26]	**0.991**	**0.961**	0.798	0.973
3D-QNet	**0.989**	**0.958**	0.801	0.965
3D-UNet [24]	**0.991**	**0.959**	**0.830**	0.964
3D-QNet-NonTensor	0.982	0.953	0.799	0.879
DRINet [27]	0.980	0.951	0.802	**0.988**
3D-ESPNet [28]	0.987	0.943	0.798	0.961

TABLE V: Average number of iterations required for convergence of the proposed 3D-QNet and 3D-QNet-NonTensor

Methods	Modality	Number of iterations			
		v_β	v_χ	v_ξ	v_κ
3D-QNet	$T1$	30.89	30.64	30.38	30.91
	$T1-CE$	31.60	31.46	31.43	31.68
	$Flair$	30.78	30.23	30.18	30.57
	$T2$	32.25	32.66	32.14	32.73
	$Liver$	27.11	27.89	26.99	27.08
3D-QNet-NonTensor	$T1$	31.46	31.59	31.43	31.69
	$T1-CE$	32.98	32.33	32.39	32.56
	$Flair$	31.69	31.12	31.19	31.26
	$T2$	32.88	32.34	32.51	32.79
	$Liver$	28.52	28.16	28.12	28.17

architecture has the potential to explore the intrinsic properties of quantum parallelism to simultaneously compute the image pixels. However, 3D-QNet is computed and experimented on a classical system, and hence the quantum parallelism has not been fully explored in the proposed quantum-inspired framework. Despite the fact that quantum simulation requires a great deal of resources in general, the proposed quantum-inspired model, 3D-QNet, requires a lesser number of parameters compared to the 3D classical CNN models.

VIII. CONCLUSION

A 3D Quantum-inspired Self-supervised Tensor Network (3D-QNet) architecture characterized by $\mathcal{S}$-connected voxel-wise processing for fully automated semantic segmentation of Brain MR volumes and 3D Liver CT scans, is presented in this work. Intensive validation using the BRATS 2019 and LiTS17 data sets shows the efficacy of the proposed self-supervised

3D-QNet architecture to promote automatic semantic segmentation of 3D medical images in real-time with minimum human intervention, still being considered as an uphill task in the field of volumetric medical image segmentation.

Despite being a 3D self-supervised network model, 3D-QNet achieved similar dice similarity score on complete tumor detection as deeply supervised 3D-UNet, Vox-ResNet, DRINet and ESPNet, thus promoting self-supervised network learning for volumetric segmentation of medical images. In principle, the proposed 3D-QNet is a general self-supervised network architecture which can be extended to many other 3D medical image segmentation avenues, where the segmented annotations are limited. Furthermore, the proposed 3D self-supervised model can be used immediately in any application (e.g., medical IoT devices) where 3D deep learning models face
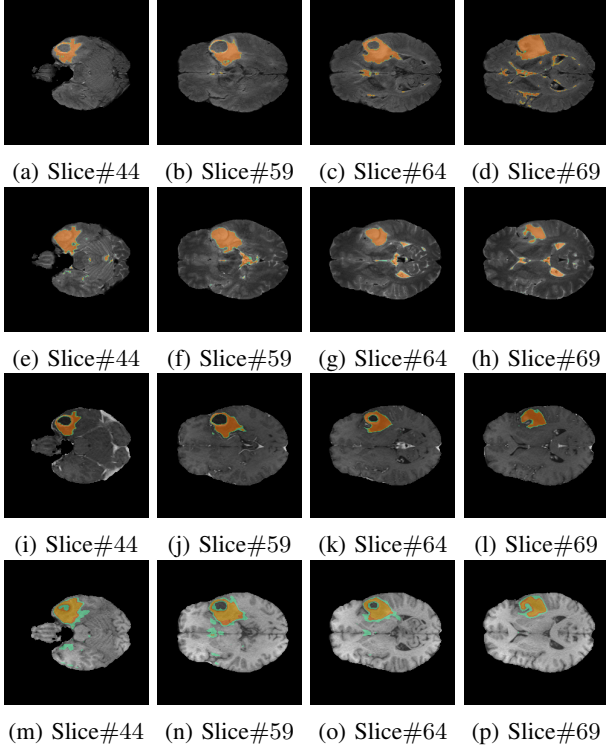
(a) Slice#44   (b) Slice#59   (c) Slice#64   (d) Slice#69

(e) Slice#44   (f) Slice#59   (g) Slice#64   (h) Slice#69

(i) Slice#44   (j) Slice#59   (k) Slice#64   (l) Slice#69

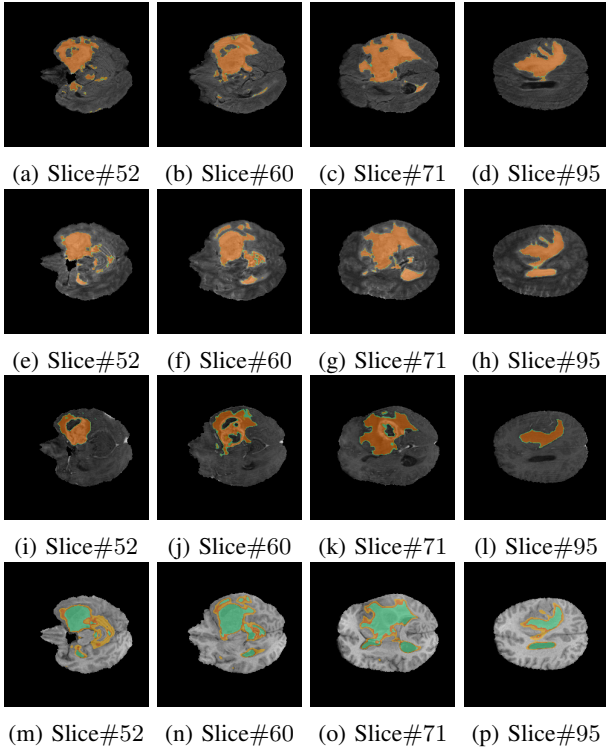(m) Slice#44   (n) Slice#59   (o) Slice#64   (p) Slice#69

Fig. 4: 3D-QNet segmented Brain MR volume $(a - d)$ BraTS19-CBICA-AAG-1-flair, $(e-h)$ BraTS19-CBICA-AAG-1-t2, $(i - l)$ BraTS19-CBICA-AAG-1-t1ce, $(m - p)$ BraTS19-CBICA-AAG-1-t1 from the BRATS 2019 data set [47] (Union of overlapped brown/yellow and green corresponds to a complete tumor (WT) region).
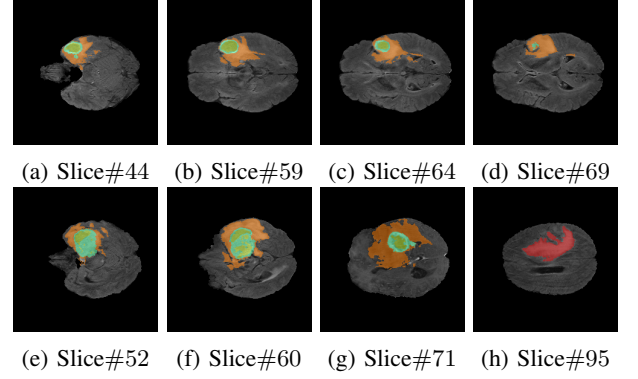
(a) Slice#52   (b) Slice#60   (c) Slice#71   (d) Slice#95

(e) Slice#52   (f) Slice#60   (g) Slice#71   (h) Slice#95

(i) Slice#52   (j) Slice#60   (k) Slice#71   (l) Slice#95

(m) Slice#52   (n) Slice#60   (o) Slice#71   (p) Slice#95

Fig. 5: 3D-QNet segmented Brain MR volume $(a - d)$ BraTS19-CBICA-AAB-1-flair, $(e-h)$ BraTS19-CBICA-AAB-1-t2, $(i - l)$ BraTS19-CBICA-AAB-1-t1ce, $(m - p)$ BraTS19-CBICA-AAB-1-t1 from the BRATS 2019 data set [47] (Union of overlapped brown/yellow and green corresponds to a complete tumor (WT) region).

(a) Slice#44   (b) Slice#59   (c) Slice#64   (d) Slice#69

(e) Slice#52   (f) Slice#60   (g) Slice#71   (h) Slice#95

Fig. 6: Annotated Brain MR volume $(a-d)$ BraTS19-CBICA-AAG-1-seg, $(e - h)$ BraTS19-CBICA-AAB-1-seg from the BRATS 2019 data set [47] (Complete tumor (WT) region comprises a union of brown, light green and green yellow, core tumor (TC) is the union of light green and green yellow, and green yellow corresponds to the tumor enhancing (TE)).
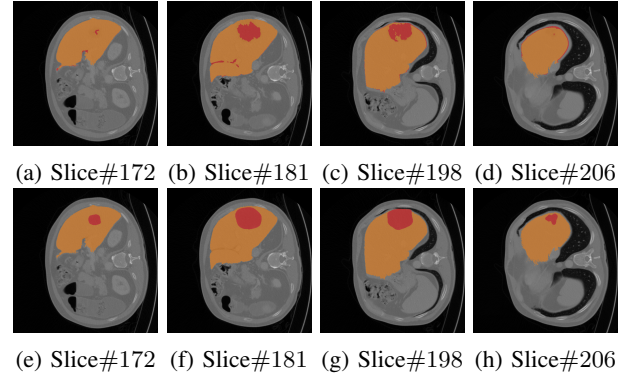
(a) Slice#172   (b) Slice#181   (c) Slice#198   (d) Slice#206

(e) Slice#172   (f) Slice#181   (g) Slice#198   (h) Slice#206

Fig. 7: $(a - d)$ 3D-QNet segmented volumetric Liver image slices (scan#64), $(e - h)$ manually segmented image slices (scan#64) from data set [48] (Union of overlapped brown and red corresponds to a complete tumor (WT) region).

significant challenges. However, the 3D-QNet fails to yield optimal outcome for multi-level segmentation on the BRATS 2019 data set. The authors are currently engaged in extending the 3D-QNet architecture by up-scaling the intermediate volumetric features in the network and optimizing its hyper-parameters to yield optimal segmentation outcome.

APPENDIX

A. Convergence Analysis of 3D-QNet

Le us assume the optimal phase angles at depth d for the weighted matrix and the activation are denoted as $\overline{\omega^d}$ and $\overline{\vartheta^d}$, respectively. Now, consider

$$\mathcal{W}^{\iota,d} = \omega^{\iota,d} - \overline{\omega^d} \tag{31}$$

$$\mathcal{V}^{\iota,d} = \vartheta^{\iota,d} - \overline{\vartheta^d} \tag{32}$$

and

$$\mathcal{D}^{\iota,d} = \omega^{\iota+1,d} - \omega^{\iota,d} = \mathcal{W}^{\iota+1,d} - \mathcal{W}^{\iota,d} \tag{33}$$

$$\mathcal{P}^{\iota,d} = \vartheta^{\iota+1,d} - \vartheta^{\iota,d} = \mathcal{V}^{\iota+1,d} - \mathcal{V}^{\iota,d} \tag{34}$$

The loss function $\zeta(\omega^{\iota,d}, \vartheta^{\iota,d})$ is differentiable with respect to $\omega^{\iota,d}$ and $\vartheta^{\iota,d}$ as

$$\frac{\partial \zeta(\omega^{\iota,d}, \vartheta^{\iota,d})}{\partial \omega_{ij}^{\iota,d}} = \frac{2}{\mathcal{N}} \sum_{i=1}^{\mathcal{N}} \sum_{j=1}^{\mathcal{S}} \triangle\varphi_{ij}^{\iota,d}(\omega_{ij}^{\iota,d}, \vartheta_j^{\iota,d})$$
$$\left[\frac{\partial \varphi_{ij}^{\iota+1,d}(\omega_{ij}^{\iota+1,d}, \vartheta_j^{\iota+1,d})}{\partial \omega_{ij}^{\iota+1,d}} - \frac{\partial \varphi_{ij}^{\iota,d}(\omega_{ij}^{\iota,d}, \vartheta_j^{\iota,d})}{\partial \omega_{ij}^{\iota,d}} \right] \tag{35}$$

$$\frac{\partial \zeta(\omega^{\iota,d}, \vartheta^{\iota,d})}{\partial \vartheta_j^{\iota,d}} = \frac{2}{\mathcal{N}} \sum_{i=1}^{\mathcal{N}} \sum_{j=1}^{\mathcal{S}} \triangle\varphi_{ij}^{\iota,d}(\omega_{ij}^{\iota,d}, \vartheta_j^{\iota,d})$$

$$\left[\frac{\partial \varphi_{ij}^{\iota+1,d}(\omega_{ij}^{\iota+1,d}, \vartheta_j^{\iota+1,d})}{\partial \vartheta_j^{\iota+1,d}} - \frac{\partial \varphi_{ij}^{\iota,d}(\omega_{ij}^{\iota,d}, \vartheta_j^{\iota,d})}{\partial \vartheta_j^{\iota,d}} \right] \quad (36)$$

where,

$$\triangle\varphi_{ij}^{\iota,d}(\omega_{ij}^{\iota,d}, \vartheta_j) = |\varphi_{ij}^{\iota+1,d}(\omega_{ij}^{\iota+1,d}, \vartheta_j^{\iota+1,d}) - \varphi_{ij}^{\iota,d}(\omega_{ij}^{\iota,d}, \vartheta_j^{\iota,d})| \quad (37)$$

The following equations evaluate the change in phase or angles ($\triangle\omega$ and $\triangle\alpha$) of the rotation gates as

$$\triangle\omega_{ij}^{\iota,d} = -\rho_{ij}^{\iota,d}\{\frac{\partial\varphi(\omega^{\iota,d}, \vartheta^{\iota,d})}{\partial\omega_{ij}^{\iota,d}}\varphi(\omega^{\iota,d}, \vartheta^{\iota,d})\}^{\frac{1}{\tau}} \quad (38)$$

$$\triangle\vartheta_j^{\iota,d} = -\kappa_j^{\iota,d}\{\frac{\partial\varphi(\omega^{\iota,d}, \vartheta^{\iota,d})}{\partial\vartheta_i^{\iota,d}}\varphi(\omega^{\iota,d}, \vartheta^{\iota,d}))\}^{\frac{1}{\tau}} \quad (39)$$

where, ρ_{ij} and κ_j refer to the learning rates for the adjustments of weights and activation, respectively and are evaluated as

$$\rho_{ij}^{\iota,d} = \mathcal{X}_i^{\iota,d} - \mathcal{X}_{ij}^{\iota,d} \forall j = 1, 2 \ldots 8$$
$$\kappa_j^{\iota,d} = (\sum_j \mathcal{X}_{i,j}^{\iota,d}) \forall j = 1, 2 \ldots 8 \quad (40)$$

The sequences of $\{\omega^{\iota,d}\}$ and $\{\vartheta^{\iota,d}\}$ converge super-linearly subject to the following conditions [15].

$$\lim_{\iota \to \infty} \frac{||\omega^{\iota+1,d} - \overline{\omega}^d||}{||\omega^{\iota,d} - \overline{\omega}^d||} \leq 1 \quad (41)$$

and

$$||\mathcal{W}^{\iota+1,d}|| = O||\mathcal{D}^{\iota,d}|| \quad (42)$$

Also,

$$\lim_{\iota \to \infty} \frac{||\vartheta^{\iota+1,d} - \overline{\vartheta}^d||}{||\vartheta^{\iota} - \overline{\vartheta}^d||} \leq 1 \quad (43)$$

and

$$||\mathcal{V}^{\iota+1,d}|| = O||\mathcal{P}^{\iota,d}|| \quad (44)$$

The convergence of the sequence $\{\omega^{\iota,d}\}$ according to L-Lipschitz continuity is illustrated as [50]

$$\zeta(\omega^{\iota+1,d}) \leq \zeta(\omega^{\iota,d}) + \langle\nabla_\omega\zeta(\omega^{\iota,d}), \omega^{\iota+1,d} - \omega^{\iota,d}\rangle + \frac{\iota}{2}||\omega^{\iota+1,d} - \omega^{\iota,d}||^2$$

$$= \zeta(\omega^{\iota,d}) + \langle\nabla_\omega\zeta(\omega^{\iota,d}) - \rho\nabla_\omega\zeta(\omega^{\iota,d})\rangle + \frac{L}{2}|| - \rho\nabla_\omega\zeta(\omega^{\iota,d})||^2$$

$$= \zeta(\omega^{\iota,d}) - \rho||\nabla_\omega\zeta(\omega^{\iota,d})||^2 + \rho^2\frac{L}{2}||\nabla_\omega\zeta(\omega^{\iota,d})||^2$$

$$= \zeta(\omega^{\iota,d}) - \rho(1 - \rho\frac{L}{2})||\nabla_\omega\zeta(\omega^{\iota,d})||^2$$

$$\leq \zeta(\omega^{\iota,d}) - \frac{\rho}{2}||\nabla_\omega\zeta(\omega^{\iota,d})||^2 \ (Assuming, \ \rho \in (0, \frac{1}{L}])$$

$$\leq \zeta(\overline{\omega}^d) + \langle\nabla_\omega\zeta(\omega^{\iota,d}), \omega^{\iota,d} - \overline{\omega}^d\rangle - \frac{\rho}{2}||\nabla_\omega\zeta(\omega^{\iota,d})||^2, \ (\zeta \ is \ convex)$$

$$= \zeta(\overline{\omega}^d) + \langle\nabla_\omega\zeta(\omega^{\iota,d}), \omega^{\iota,d} - \overline{\omega}^d\rangle - \frac{\rho}{2}||\nabla_\omega\zeta(\omega^{\iota,d})||^2 + \frac{1}{2\rho}(||\omega^{\iota,d} - \overline{\omega}^d||^2 - ||\omega^{\iota,d} - \overline{\omega}^d||^2)$$

$$= \zeta(\overline{\omega}^d) + \frac{1}{2\rho}(||\omega^{\iota,d} - \overline{\omega}^d||^2 - (||\omega^{\iota,d}||^2 - 2\langle\omega^{\iota,d}, \overline{\omega}^d\rangle + ||\overline{\omega}^d||^2 - 2\rho\langle\nabla_\omega\zeta(\omega^{\iota,d}), \omega^{\iota,d} - \overline{\omega}^d\rangle + \rho^2||\nabla_\omega\zeta(\omega^{\iota,d})||^2))$$

$$= \zeta(\overline{\omega}^d) + \frac{1}{2\rho}(||\omega^{\iota,d}|| - \overline{\omega}^d||^2 - (||\omega^{\iota,d} - \rho\nabla_\omega\zeta(\omega^{\iota,d})||^2 - 2\langle\omega^{\iota,d} - \nabla_\omega\zeta(\omega^{\iota,d}), \overline{\omega}^d\rangle + ||\overline{\omega}^d||^2))$$

$$= \zeta(\overline{\omega}^d) + \frac{1}{2\rho}(||\omega^{\iota,d} - \overline{\omega}^d||^2 - ||\omega^{\iota+1,d} - \overline{\omega}^d||^2)$$

$$\therefore, \zeta(\omega^{\iota+1,d}) - \zeta(\overline{\omega}^d) \leq \frac{1}{2\rho}(||\omega^{\iota,d} - \overline{\omega}^d||^2 - ||\omega^{\iota+1,d} - \overline{\omega}^d||^2)$$

Similarly, it can also be shown that

$$\zeta(\vartheta^{\iota+1,d}) - \zeta(\overline{\vartheta}^{,d}) \leq \frac{1}{2\rho}(||\vartheta^{\iota+1,d} - \overline{\vartheta}^d||^2 - ||\vartheta^{\iota+1,d} - \overline{\vartheta}^d||^2) \quad (45)$$

Now, according to Thaler formula

$$\zeta(\omega^{\iota+1,d}, \vartheta^{\iota+1,d}) - \zeta(\omega^{\iota,d}, \vartheta^{\iota,d}) = \quad (46)$$

$$\begin{bmatrix} \triangle\omega_{ij}^{\iota,d} & \triangle\vartheta_j^{\iota,d} \end{bmatrix} \begin{bmatrix} \frac{\partial\zeta(\omega^{\iota,d}, \vartheta^{\iota,d})}{\partial\omega_{ij}^{\iota,d}} \\ \frac{\partial\zeta(\omega^{\iota,d}, \vartheta^{\iota,d})}{\partial\vartheta_j^{\iota,d}} \end{bmatrix} + O\begin{bmatrix} ||\triangle\omega_{ij}^{\iota,d} & \triangle\vartheta_i^{\iota,d}|| \end{bmatrix}$$

$$\approx \left[\{-\rho_{ij}^{\iota,d}\frac{\partial\zeta(\omega^{\iota,d}, \vartheta^{\iota,d})}{\partial\omega_{ij}^{\iota,d}}\}^2 + \{-\kappa_j^{\iota,d}\frac{\partial\zeta(\omega^{\iota,d}, \vartheta^{\iota,d})}{\partial\vartheta_j^{l,d}}\}^2 \right] \{\zeta(\omega^{\iota,d}, \vartheta^{\iota,d})\}^{\frac{1}{\iota}} \quad (47)$$

It is obvious that $(\zeta(\omega^{\iota+1,d}, \alpha^{\iota+1,d}) - \zeta(\omega^{\iota,d}, \vartheta^{\iota,d})) \leq 0$ and the sequences of $\{\omega^{\iota,d}\}$ and $\{\vartheta^{\iota,d}\}$ are monotonically decreasing as

$$\lim_{\iota \to \infty} \zeta(\omega^{\iota,d}, \vartheta^{\iota,d}) = (\overline{\omega}^d, \overline{\vartheta}^d) \quad (48)$$

and

$$\lim_{\iota \to \infty} \frac{||\zeta(\omega^{\iota+1,d}, \vartheta^{\iota+1,d}) - (\overline{\omega}^d, \overline{\vartheta}^d)||}{||\zeta(\omega^{\iota,d}, \vartheta^{\iota,d}) - (\overline{\omega}^d, \overline{\vartheta}^d)||} \leq 1 \quad (49)$$

B. Code Availability

3D-QNet implementation is made available in GitHub: https://github.com/konar1987/3D-QNet for brain volume image segmentation with few samples, tailored and tested for *FLAIR* and *T2* from the BRATS 2019 data set [47].

REFERENCES

[1] G. Litjens *et al.*, "A survey on deep learning in medical image analysis," *Medical Image Analysis*, vol. 42, pp. 60—88, 2017. doi: https://doi.org/10.1016/j.media.2017.07.005.

[2] M. Huang, W. Yang, Y. Wu, J. Jiang, W. Chen, and Q. Feng, "Brain Tumor Segmentation Based on Local Independent Projection-Based Classification," *IEEE Transactions on Biomedical Engineering*, vol. 61, no. 10, pp. 2633–2645, 2014, doi: 10.1109/TBME.2014.2325410.

[3] Z. Wu, K. D. Paulsen, and J. M. Sullivan, "Adaptive model initialization and deformation for automatic segmentation of T1-weighted brain MRI data", *IEEE Transactions on Biomedical Engineering*, vol. 52, no. 6, pp. 1128–1131, 2005, doi: 10.1109/TBME.2005.846709.

[4] M. Chung, J. Lee, M. Lee, J. Lee, Y-G. Shin, "Deeply self-supervised contour embedded neural network applied to liver segmentation," *Computer Methods and Programs in Biomedicine*, vol. 192, pp. 105447, 2020, https://doi.org/10.1016/j.cmpb.2020.105447.

[5] F. Milletari, N. Navab, and S. A. Ahmadi, "V-Net: Fully Convolutional Neural Networks for Volumetric Medical Image Segmentation" *2016 Fourth International Conference on 3D Vision (3DV)*, pp. 565--571, 2016 doi:10.1109/3DV.2016.79.

[6] O. Ronneberger, P. Fischer, T. Brox, "U-Net: convolutional networks for biomedical image segmentation. *International Conference on Medical Image Computing and Computer-Assisted Intervention (MICCAI 2015)*, vol. 9351, pp. 234--241. 2016. doi: https://doi.org/10.1007/978-3-319-46723-8_4.

[7] Q. Doua, L. Yua, H. Chena, Y.Jina, X. Yanga, J. Q. Pheng, and A. Heng, "3D deeply supervised network for automated segmentation of volumetric medical images," *Medical Image Analysis*, vol. 41, pp. 40–54, 2017, doi: https://doi.org/10.1016/j.media.2017.05.001.

[8] V. Gandhi, G. Prasad, D. Coyle, L. Behera, and T. M. McGinnity, "Quantum neural network-based EEG filtering for a brain-computer interface," *IEEE Transaction on Neural Network and Learning Systems*, vol. 25, no. 2, pp. 278--288, 2014, doi: 10.1109/TNNLS.2013.2274436.

[9] P. Li, H. Xiao, F. Shang, X. Tong, X. Li, and M. Cao, "A hybrid quantum-inspired neural networks with sequence inputs," *Neurocomputing*, vol. 117, pp. 81--90, 2013, doi: https://doi.org/10.1016/j.neucom.2013.01.029.

[10] N. Masuyama, C. K. Loo, M. Seera, and N. Kubota, "Quantum-Inspired Multidirectional Associative Memory With a Self-Convergent Iterative Learning," *IEEE Transaction on Neural Network and Learning Systems*, vol. 29, no. 4, pp. 1058—1068, 2018, doi: 10.1109/TNNLS.2017.2653114.

[11] S. Bhattacharyya, P. Pal and S. Bhowmick, "Binary Image Denoising Using a Quantum Multilayer Self Organizing Neural Network," *Applied Soft Computing*, vol. 24, pp. 717–729, 2014, doi: https://doi.org/10.1016/j.asoc.2014.08.027.

[12] M. Mediouni, D. R. Schlatterer, H. Madry, M. Cucchiarini and B. Rai, "A review of translational medicine. The future paradigm: how can we connect the orthopedic dots better?," *Current Medical Research and Opinion*, vol. 34, no. 7, pp. 1217–1229, 2018, doi: 10.1080/03007995.2017.1385450.

[13] M. Mediouni, R. Madiouni, M. Gardner, N. Vaughan, Neil, "Translational medicine: Challenges and new orthopaedic vision (Mediouni-Model)," *Current Orthopaedic Practice*, vol. 31. no. 2, pp. 196-200, 2020, doi: 10.1097/BCO.0000000000000846.

[14] D. Konar, S. Bhattacharyya, T. K. Gandhi and B. K. Panigrahi, "A quantum-inspired self-supervised Network model for automatic segmentation of brain MR images," *Applied Soft Computing*, vol. 93, 2020, doi: https://doi.org/10.1016/j.asoc.2020.106348.

[15] D. Konar, S. Bhattacharyya, B. K. Panigrahi and E. C. Behrman, "Qutrit-Inspired Fully Self-Supervised Shallow Quantum Learning Network for Brain Tumor Segmentation," *IEEE Transactions on Neural Networks and Learning Systems*, vol. 33, no. 11, pp. 6331–6345, Nov. 2022, doi: 10.1109/TNNLS.2021.3077188.

[16] M. Havaei *et al.*, "Brain tumor segmentation with deep neural networks," *Medical Image Analysis*, vol. 35, pp. 18–31, 2017, doi: https://doi.org/10.1016/j.media.2016.

[17] E. Shelhamer, J. Long, and T. Darrell, "Fully convolutional networks for semantic segmentation," *IEEE Transactions on Pattern Analysis and Machine Intelligence*, vol. 39, no. 4, pp. 640–651, 2017, doi: 10.1109/TPAMI.2016.2572683.

[18] S. Pereira, A. Pinto, V. Alves, and C. A. Silva, "Brain Tumor Segmentation Using Convolutional Neural Networks in MRI Images," *IEEE Transactions on Medical Imaging*, vol.35, no. 5, 2016, doi: 10.1109/TMI.2016.2538465.

[19] P. Moeskops, M. A. Viergever, A. M. Mendrik, L. S. Vries, M. J. N. L. Benders and I. Išgum, "Automatic Segmentation of MR Brain Images With a Convolutional Neural Network,"*IEEE Transactions on Medical Imaging*, vol.35, no.5, 2016, doi: 10.1109/TMI.2016.2548501.

[20] G. Wang *et al.*, "DeepIGeoS: A Deep Interactive Geodesic Framework for Medical Image Segmentation," *IEEE Transactions on Pattern Analysis and Machine Intelligence*, vol. 41, no. 7, pp. 1559–1572, 2019, doi: 10.1109/TPAMI.2018.2840695.

[21] S. Banerjee, L. Magee, D. Wang *et al.*, "Semantic segmentation of microscopic neuroanatomical data by combining topological priors with encoder–decoder deep networks," *Nature Machine Intelligence*, vol. 2, pp. 585—594, 2020, doi: https://doi.org/10.1038/s42256-020-0227-9.

[22] K. Kamnitsas, "Efficient multi-scale 3D CNN with fully connected CRF for accurate brain lesion segmentation," *Medical Image Analysis*, vol. 36, pp. 61–78, 2017, doi: https://doi.org/10.1016/j.media.2016.10.004.

[23] Q. Dou, H. Chen, L. Yu, L. Zhao, J. Qin, D. Wang, V. C. Mok, L. Shi, and P. A. Heng. "Automatic Detection of Cerebral Microbleeds From MR Images via 3D Convolutional Neural Networks, *IEEE Transactions on Medical Imaging*, vol. 35, no. 5, pp. 1182-–1195, 2016, doi: 10.1109/TMI.2016.2528129.

[24] Ö. Çiçek, A. Abdulkadir, S. S. Lienkamp, T. Brox, and O. Ronneberger, "3D U-Net: Learning Dense Volumetric Segmentation from Sparse Annotation," *International Conference on Medical Image Computing and Computer-Assisted Intervention (MICCAI 2016)*, pp. 424-–432, 2016, doi: https://doi.org/10.1007/978-3-319-46723-8_49.

[25] A. Brebisson, and G. Montana, "Deep Neural Networks for Anatomical Brain Segmentation," *In: Proceedings of the IEEE Conference on Computer Vision and Pattern Recognition Workshops*, pp. 20-–28, 2015, doi: 10.1109/CVPRW.2015.7301312.

[26] H. Chen, Q. Dou, L. Yu, J. Qin, and P. A. Heng, 2017. "VoxResNet: Deep voxelwise residual networks for brain segmentation from 3D MR images," *NeuroImage*, vol. 170, pp. 446-455, 2017, doi: https://doi.org/10.1016/j.neuroimage.2017.04.041.

[27] L.Chen , P. Bentley, K. Mori, K. Misawa, M. Fujiwara, and D. Rueckert, "DRINet for Medical Image Segmentation," *IEEE Transaction on Medical Imaging*, vol. 37, no. 11, 2018, doi: 10.1109/TMI.2018.2835303.

[28] N. Nuechterlein and S. Mehta, "3D-ESPNet with Pyramidal Refinement for Volumetric Brain Tumor Image Segmentation," *International MICCAI Brainlesion Workshop (BrainLes 2018)*, pp. 245–253, 2018, doi: https://doi.org/10.1007/978-3-030-11726-9_22.

[29] G. Wang *et al.*, "Interactive Medical Image Segmentation Using Deep Learning With Image-Specific Fine Tuning," *IEEE Transactions on Medical Imaging*, vol. 37, no. 7, 2018, doi: 10.1109/TMI.2018.2791721.

[30] N. Tajbakhsh *et al.*, "Convolutional Neural Networks for Medical Image Analysis: Full Training or Fine Tuning?," *IEEE Transactions on Medical Imaging*, vol. 35, no. 5, pp. 1299–1312, 2016, doi: 10.1109/TMI.2016.2535302.

[31] X. Zhuang, Y. Li, Y. Hu, K. Ma, Y. Yang, and Y. Zheng, "Self-supervised Feature Learning for 3D Medical Images by Playing a Rubik's Cube," *International Conference on Medical Image Computing and Computer-Assisted Intervention (MICCAI 2019)*, pp. 420–428, https://doi.org/10.1007/978-3-030-32251-9_46.

[32] M. Blendowski, H. Nickisch, M. P. Heinrich, "How to Learn from Unlabeled Volume Data: Self-supervised 3D Context Feature Learning," Proc. Medical Image Computing and Computer Assisted Intervention – MICCAI 2019, vol 11769, 2019, https://doi.org/10.1007/978-3-030-32226-7_72.

[33] A. Ghosh, N. R. Pal, and S. K. Pal, "Self organization for object extraction using a multilayer neural network and fuzziness measures," *IEEE Transactions on Fuzzy Systems*, vol. 1, no.1, pp. 54–68, 1993, doi: 10.1109/TFUZZ.1993.390285.

[34] S. Bhattacharyya, P. Dutta and U. Maulik, "A parallel bi-directional self-organizing neural network (PBDSONN) architecture for color image extraction and segmentation," *Neurocomputing*, vol. 86, pp. 1–23, 2012, doi: https://doi.org/10.1016/j.neucom.2011.11.025.

[35] G. Purushothaman, N. B. Karayiannis, "Quantum neural networks (QNNs): inherently fuzzy feedforward neural networks," *IEEE Transactions on Neural Networks*, vol. 8 , no. 3, 1997, doi: 10.1109/72.572106.

[36] T. C. Lu, G. R. Yu, and J. C. Juang, "Quantum-based algorithm for optimizing artificial neural networks," *IEEE Transaction on Neural Network and Learning Systems*, vol. 24, no. 8, pp. 1266—1278, 2013, doi: 10.1109/TNNLS.2013.2249089.

[37] Nam-H. Nguyen ; E. C. Behrman, A. Moustafa, J. E. Steck, "Benchmarking Neural Networks For Quantum Computations," *IEEE Transactions on Neural Networks and Learning Systems*, pp. 1-10, 2019, doi:10.1109/TNNLS.2019.2933394.

[38] E. M. Stoudenmire, and D. J. Schwab, "Supervised Learning with Quantum-Inspired Tensor Networks," *https://www.arxiv-vanity.com/papers/1605.05775/*, 2020.

[39] D. Konar, S. Bhattacharya, B. K. Panigrahi, K. Nakamatsu "A quantum bi-directional self-organizing neural network (QBDSONN) architecture for binary object extraction from a noisy perspective," *Applied Soft Computing*, vol.46, pp. 731–752, 2016, doi: https://doi.org/10.1016/j.asoc.2015.12.040.

[40] D. Konar, S. Bhattacharya, U. Chakraborty, T. K.Gandhi, B. K. Panigrahi, "A quantum parallel bi-directional self-organizing neural network (QPBDSONN) architecture for extraction of pure color objects from noisy background," *Proc. IEEE International Conference on Advances in Computing, Communications and Informatics (ICACCI), 2016*, pp. 1912–1918, 2016, doi: 10.1109/ICACCI.2016.7732330.

[41] D. Konar, S. Bhattacharyya and B. K. Panigrahi, "QIBDS Net: A Quantum-Inspired Bi-Directional Self-supervised Neural Network Architecture for Automatic Brain MR Image Segmentation," *Proc. 8th International Conference on Pattern Recognition and Machine Intelligence (PReMI 2019)*, vol. 11942, pp. 87–95, 2019, doi:https://doi.org/10.1007/978-3-030-34872-4_64.

[42] M. A. Nielson and I. L. Chung, *Quantum computation and quantum information*, Cambridge University press, 2002.

[43] T. G. Kolda, B. W. Bader, "Tensor Decompositions and Applications," *SIAM Review*, vol. 51, no. 3, pp. 455-–500, 2009, doi: https://doi.org/10.1137/07070111X.

[44] S. Bhattacharyya, P. Dutta and U. Maulik, "Multilevel image segmentation with adaptive image context based thresholding," *Applied Soft Computing*, vol. 11, no.1, pp. 946–962, 2011, doi: https://doi.org/10.1016/j.asoc.2010.01.015.

[45] N. Otsu, "A threshold selection method from gray level histograms," *IEEE Transactions on Systems, Man, and Cybernetics*, vol. 9, no. 1, pp. 62–66, 1979, doi: 10.1109/TSMC.1979.4310076.

[46] H. P. Ng, S. H. Ong, K. W. C. Foong, P. S. Goh, and W. L. Nowinski, "Medical Image Segmentation Using K-Means Clustering and Improved Watershed Algorithm," *2006 IEEE Southwest Symposium on Image Analysis and Interpretation*, 2006, doi: 10.1109/SSIAI.2006.1633722.

[47] B. H. Menze *et al.*, "The multimodal brain tumor image segmentation benchmark (BRATS)," *IEEE Transactions on Medical Imaging*, vol. 34, no. 10, pp. 1993-–2024, 2015, doi: 10.1109/TMI.2014.2377694.

[48] P. Bilic *et al.*, "The Liver Tumor Segmentation Benchmark (LiTS)," *arXiv*, 2019, arXiv:1901.04056.

[49] M. H. Gail and S. B. Green, "Critical values for the one-sided two-sample Kolmogorov–Smirnov statistic," *J. Am. Stat. Assoc.*, vol. 71, pp. 757–760, 1976.

[50] H. Kim, J. Kang, W. Park, S. Ko, Y. Cho, D. Yu, Y. Song, and J. Choi, "Convergence Analysis of Optimization Algorithms," 2017, arXiv:1707.01647.